Materials Advances

ROYAL SOCIETY OF CHEMISTRY

PAPER

View Article Online
View Journal | View Issue

Cite this: *Mater. Adv.*, 2026, 7, 1519

Single-host white light emission in self-activated $Rb_{3-x}Cs_xY_{1-y}Bi_yV_2O_8$: crystal engineering for high-performance indoor lighting

J. S. Revathy,†[a] Monalisha Behera, †[b] Shisina S,†[ad] Jatin Dhanuka,[b] Sudipta Som, *[b] R. K. Dubey[c] and Subrata Das *[ad]

In our quest to replicate the full spectrum of natural daylight, which creates comfortable and visually stimulating reading environments, we have engineered a novel single-component phosphor based on divanadate compounds. Traditional broadband yellow-emitting rare-earth garnet systems often underperform due to insufficient emission in the red and cyan regions, delivering light with noticeable spectral gaps and cooler tones that can strain the eyes during prolonged reading. This tailored approach replaces rubidium with cesium and strategically incorporates bismuth into the $Rb_{3-x}Cs_xYV_2O_8$ matrix, inducing fine crystal field modifications that boost luminescence intensity and generate a warm white emission. The altered light output effectively minimizes the drawbacks of multi-phosphor assemblies, offering a streamlined solution that overcomes issues such as high correlated color temperatures and poor color fidelity. The $Cs_3Bi_{0.25}Y_{0.75}V_2O_8$ composition exhibits high thermal stability, retaining 75% of its emission intensity at 423 K, with a robust activation energy of 0.32 eV. When integrated into LED devices, the phosphor demonstrates a remarkable ability to shift the white emission from cooler ($Cs_3YV_2O_8$: CCT ≈ 6111 K, CRI ≈ 78) to warmer hues ($Cs_3Bi_{0.25}Y_{0.75}V_2O_8$: CCT ≈ 4887 K, CRI ≈ 79). In particular, the rare-earth-free $Cs_3BiV_2O_8$ composition-based white LED emits white light CCT ≈ 4662 K, closely emulating the soft, balanced glow of natural sunlight. Such spectral tuning enhances visual clarity and minimizes eye fatigue, creating an inviting atmosphere ideal for reading rooms and workspaces. This study underscores the potential of precise crystal engineering and controlled doping strategies in developing high-performance lighting solutions that set a new benchmark for indoor illumination, mirroring the natural radiance of the sun.

Received 14th August 2025,
Accepted 3rd December 2025

DOI: 10.1039/d5ma00905g

rsc.li/materials-advances

1. Introduction

Lighting plays a crucial role in shaping our indoor environments, especially in spaces designed for reading and focused work. The quality of light affects not only visibility but also eye comfort and cognitive performance.[1–3] In pursuit of optimal artificial lighting, researchers have explored various materials and technologies to mimic natural sunlight, the gold standard for illumination. In modern phosphor LED lighting, yttrium–aluminum–garnet (YAG) is the most famous material that, when combined with blue InGaN LEDs (λ_{ex} ≈ 450 nm), produces white light. Commercial YAG-based pc-WLEDs utilize a two-component system, where a blue LED serves as the excitation source and the yellow-emitting YAG:Ce phosphor (λ_{em} ≈ 550 nm) converts part of the blue light into a broader spectrum.[4–6] However, these WLEDs typically exhibit a high correlated color temperature (CCT > 6500 K) and a low color rendering index (CRI < 75) due to the absence of cyan and red spectral gaps.[7,8] To overcome these limitations, researchers introduced a dual-phosphor system by combining YAG:Ce with $Sr_2Si_5N_8$:Eu^{2+}.[9,10] The incorporation of $Sr_2Si_5N_8$:Eu^{2+} effectively fills the red gap and enables the fabrication of WLEDs with an efficient CCT above 4000 K and an improved CRI approaching 85, making the light output warmer.[11,12] While effective, this dual-material system has limitations. The added complexity of fabricating two phosphors increases the production costs and manufacturing challenges. Nevertheless, the cyan gap problem persists, contributing to imbalanced color rendering and spectral deficiencies that can make the produced light less comfortable for reading environments. An ideal solution would be to achieve

[a] *Materials Science and Technology Division, CSIR-National Institute for Interdisciplinary Science and Technology (NIIST), Thiruvananthapuram, Kerala 695019, India. E-mail: subratadas.niist@csir.res.in*
[b] *School of Science and Humanities, Shiv Nadar University Chennai, Tamil Nadu 603110, India. E-mail: sudiptasom@snuchennai.edu.in*
[c] *Ind Research and development house Pvt Ltd., Sector-6, Noida-201301, UP, India*
[d] *Academy of Scientific and Innovative Research (AcSIR), Ghaziabad-201002, India*
† These authors contributed equally.

high-quality white light emission using a single material, thereby simplifying production while maintaining excellent optical properties.[13]

The motivation behind our research is to develop a single-material phosphor that can generate white light with a spectrum closely resembling that of natural sunlight. Sunlight is considered the best light source for reading rooms because of its continuous and broad spectral distribution, which ensures optimal color rendering and reduces eye strain. Unlike artificial light sources that may have gaps or spikes in their emission spectra, sunlight provides a smooth and balanced spectrum, making reading and visual tasks more comfortable.[14,15] Our goal is to design a lighting material that brings us as close as possible to this natural standard. Over the years, several luminescent materials have been studied for white light generation. YAG:Ce (yttrium aluminum garnet doped with cerium) is the most commonly used phosphor in white LEDs due to its high efficiency and stability. However, as mentioned earlier, it requires combination with a blue LED, which can lead to spectral deficiencies, especially in the red wavelength region. This can result in poor color rendering and an unnatural lighting experience. To overcome these limitations, researchers have explored various red-emitting phosphors to complement YAG:Ce-based lighting systems. Several novel phosphors have been investigated, including Eu^{3+}-activated $Ca_2RF_4PO_4$ (R = Gd, Y) and Y_2MoO_6:Eu^{3+}, which exhibit strong red emission under near-UV excitation.[16,17] These phosphors exhibit efficient absorption of near-ultraviolet or blue light and emit red light with peak wavelengths around 611 nm. Another promising phosphor, $Sr_2Si_5N_8$:Eu^{2+}, has demonstrated robust thermal performance and improved color rendering when combined with blue LEDs and the YAG:Ce phosphor.[18] The $Sr_2Si_5N_8$:Eu^{2+} phosphor demonstrated excellent thermal stability, with only a 28% power reduction at 150 °C. When combined with blue LEDs and YAG:Ce phosphor, the material achieved a CRI of 72, making it a valuable addition to solid-state lighting applications.[9–12,19] Additionally, materials like $KSrPO_4$:Eu^{2+} and $Sr_2Si_5N_8$:Eu^{2+} have demonstrated multi-wavelength emission, making them potential candidates for single-material lighting solutions.[20–22] These materials exhibit broadband emission, mimicking the natural light spectrum more effectively than traditional dual-material systems. Luminescence wavelengths play a crucial role in determining light quality. The human eye perceives light in the visible spectrum (approximately 400–700 nm), with optimal reading comfort achieved under a balanced emission across this range. Sunlight provides a near-uniform distribution of wavelengths, ensuring that no particular color dominates the spectrum. Many commercial LEDs, on the other hand, have strong peaks in the blue region (around 450 nm) and weaker emissions in the red region (above 600 nm), leading to potential eye fatigue.[23] To design an ideal reading-room lighting system, a phosphor material that emits across the full visible spectrum with a warm and balanced color temperature, closely resembling daylight, is necessary.

In the present research, first, we have synthesized highly efficient divanadate compounds $Rb_{3-x}Cs_xYV_2O_8$ using the solid-state synthesis method. Photoluminescence (PL) studies reveal broad excitation (300–400 nm, peaked at 365 nm) and emission (400–650 nm, peaked at 500 nm) due to VO_4^{3-} charge-transfer band transitions. On exploring the transition from Rb^+ to Cs^+, we observed a significant PL intensity enhancement. Cs^+ substitution modified the electronic structure and altered the local crystal field environment, improving the luminescence efficiency. Motivated by this, we introduced Bi^{3+} into the system, synthesizing $Cs_3Bi_{1-x}Y_xV_2O_8$ (x = 0 to 1). The PL spectra revealed a substantial intensity increase with Bi^{3+} incorporation, suggesting its profound influence on the electronic environment. A redshift in the PL spectra indicated modifications in bond length and electronic interactions, systematically tuning luminescence behavior. The optimized $Cs_3Bi_{0.25}Y_{0.75}V_2O_8$ enables emission tuning from cool white (6557 K) to soft hued white (4887 K), which becomes softer in the case of $Cs_3BiV_2O_8$ (CCT ≈ 4462 K), which is appropriate for indoor lighting. The balanced spectral emission ensures comfortable reading conditions, reducing eye strain and enhancing cognitive performance.

2. Materials and methods

The $Rb_{3-x}Cs_xYV_2O_8$ (x = 0–3) and $Cs_3Bi_yY_{1-y}V_2O_8$ (y = 0–1) compounds were prepared using a solid-state reaction approach. High-purity precursors, including Rb_2CO_3 (99.99%), Cs_2CO_3 (99.99%), NH_4VO_3 (99.99%), Y_2O_3 (99.99%), and Bi_2O_3 (99.99%), were measured in stoichiometric proportions. These materials were thoroughly ground in an agate mortar with ethanol for 30–45 min to ensure homogeneity. The mixture was then dried and transferred into an alumina crucible. The crucible was heated in a muffle furnace at 750 °C for 20 h in an air atmosphere. After calcination, the samples were cooled naturally to ambient temperature.[24]

The phase purity and crystalline structure of the synthesized compounds were examined using X-ray powder diffraction (XRD) on a 3rd Generation Empyrean diffractometer (Malvern Panalytical) with Cu-Kα radiation. The crystal structure was visualized and modelled using VESTA software. Photoluminescence (PL) excitation and emission spectra were obtained using a Yvon Fluorolog-3 spectrofluorometer equipped with a 450 W Xenon flash lamp as the excitation source. Temperature-dependent PL spectra and electroluminescence data were collected using an Ocean Optics spectrophotometer (Maya 2000 Pro) with 410 nm LEDs for excitation. Near-infrared phosphor-converted LED (NIR pc-LED) devices were assembled by evenly coating a blend of optimized phosphor and resin in a specific ratio onto LED chips.

3. Results and discussion

3.1. Structure evaluations

The XRD patterns of $Rb_{3-x}Cs_xYV_2O_8$ (x = 0 to 3) are shown in Fig. 1(a). The XRD spectrum of $Rb_{3-x}Cs_xYV_2O_8$ at x = 0 [$Rb_3YV_2O_8$] exhibits a strong correlation with the standard diffraction data (JCPDS No: 00-035-0279), confirming the material's crystallinity and phase purity. The result indicates that $Rb_3YV_2O_8$ adopts a trigonal structure with lattice parameters

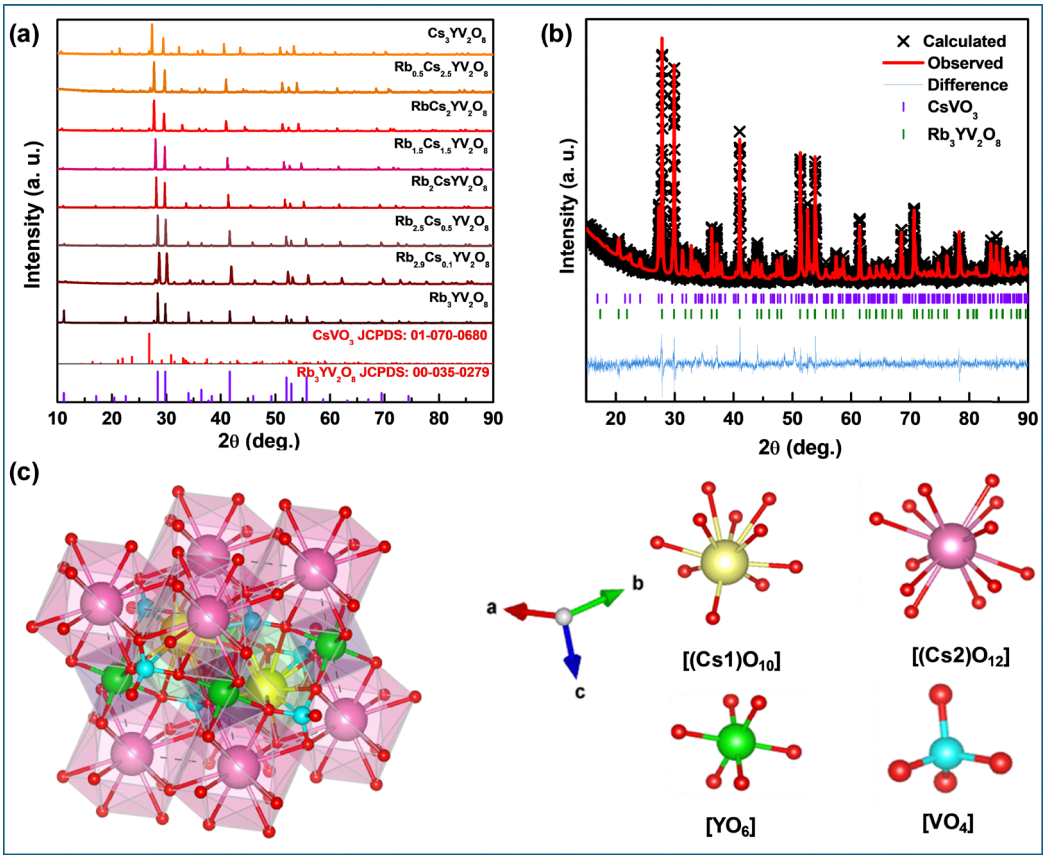

Fig. 1 (a) XRD patterns of $Rb_{3-x}Cs_xYV_2O_8$ with varying Cs concentrations from $x = 0$ to $x = 3$, (b) the Rietveld refined pattern and (c) the crystal structure of $Cs_3YV_2O_8$.

$a = b = 5.984$ Å and $c = 8.309$ Å, $\alpha = \beta = 90^\circ$ and $\gamma = 120^\circ$ belonging to the $P\bar{3}m1$ space group.[24]

As cesium (Cs) was progressively substituted for rubidium (Rb) in the $Rb_{3-x}Cs_xYV_2O_8$ system (for $x = 0$ to 3), the diffraction peaks shifted slightly to lower angles, indicating subtle changes in the lattice parameters.[25] The progressive reduction and eventual disappearance of a minor diffraction peak provided additional evidence supporting the complete substitution of rubidium (Rb) by cesium (Cs) in the crystal structure. Notably, the diffraction peak observed at 11.2°, which is characteristic of the presence of Rb, gradually fades as the concentration of Cs increases. This trend is consistent with the replacement of the smaller Rb ions by the comparatively larger Cs ions, indicating successful incorporation of Cs into the lattice. Furthermore, with increasing Cs content, a few weak diffraction peaks corresponding to $CsVO_3$ begin to emerge (with the phase fraction of $<5\%$), suggesting the possible formation of secondary phases associated with Cs at higher doping levels.

To gain deeper insights into the host crystal structure that influences the luminescence behaviours of the obtained phosphors, Rietveld refinement was carried out using the GSAS software. The Rietveld refinement plot of $Cs_3YV_2O_8$, shown in Fig. 1(b), indicates the successful formation of a single-phase phosphor with the $P\bar{3}m1$ space group having a trigonal structure, consistent with the crystal structure of $Rb_3YV_2O_8$. The quality of the refinement is assessed by the reliability factors, including the weighted pattern ($R_{wp} \sim 15.84\%$), the pattern ($R_p \sim 11.75\%$), and the goodness of fit ($\chi^2 \sim 1.35$). The corresponding parameters are summarized in Table 1. The fractional atomic coordinates of $Cs_3YV_2O_8$, in units of lattice constants, are provided for all atoms in Table 2.

Based on Rietveld refinement results, the schematic crystal structure of $Cs_3YV_2O_8$, which features a trigonal structure, is illustrated in Fig. 1(c). The crystal structure of $Cs_3YV_2O_8$ consists of a three-dimensional polyhedral framework composed of $[(Cs_1)O_{10}]$, $[(Cs_2)O_{12}]$, octahedral $[(Y)O_6]$, and tetrahedral VO_4^{3-} units interconnected through edge- and corner-sharing polyhedra.

Table 1 Refined crystallographic parameters for $Cs_3YV_2O_8$

Chemical formula	$Cs_3YV_2O_8$
Crystal structure	Trigonal
Space group	$P\bar{3}m1$
Z	1
$a = b$ (Å)	6.078 (10)
c (Å)	8.309 (7)
V (Å)^3	265.886 (5)
$\alpha = \beta$	90°
γ	120°
GOF	1.35
R_p (%)	11.75
R_{wp} (%)	15.84

Table 2 The atomic coordinates and fraction of occupancy of the $Cs_3YV_2O_8$ luminescence emitter

Atoms	Name	x	y	z	Occupancy
Cs	Cs1	0.33333	0.66667	0.70154	1
Cs	Cs2	0.00000	0.000000	0.00000	1
Y	Y3	0.00000	0.00000	0.50000	1
V	V3	0.33333	0.66667	0.25493	1
O	O4	0.17575	0.35150	0.33115	1
O	O5	0.33333	0.66667	0.04474	1

This arrangement aligns with the "bracelets and pinwheels" model proposed by Moore.[26] For orthovanadate compounds of similar structure, the pinwheel unit comprises $[YO_6]$ octahedra and $[VO_4]$ tetrahedra. Each $[YO_6]$ octahedron shares six corners with alternating $[VO_4]$ tetrahedra, forming layered structures through these connections. Cs^+ cations are situated between these layers, stabilizing the framework. When observed along the *c*-axis and *a*-axis, a single $[VO_4]$ tetrahedron is corner-linked to three $[YO_6]$ octahedra and edge-connected to two $[(Cs_2)O_{12}]$ and one $[(Cs_1)O_{10}]$ polyhedra, strengthening the structural integrity of the network.[24,27]

3.2. Optical properties

The diffuse reflectance (DR) study was conducted to explore the optical properties of the synthesized phosphors. Fig. 2(a) represents the DR spectra of $Rb_{3-x}Cs_xYV_2O_8$ (x = 0; $Rb_3YV_2O_8$ and x = 3; $Cs_3YV_2O_8$), demonstrating two absorption bands: one broad absorption ranging from 250 to 350 nm and another around 400 nm. A similar absorption band has been observed in several vanadate materials, indicating a common optical transition mechanism within this class of compounds. The broad absorption can be attributed to the electronic transition from the oxygen 2p (O 2p) orbitals to the vanadium 3d (V 3d) orbitals within the VO_4^{3-} tetrahedral groups. This charge transfer process is characteristic of vanadate-based phosphors and is responsible for their strong absorption in the ultraviolet (UV) and near-ultraviolet (n-UV) regions. The broad nature of the absorption band arises from the extensive delocalization of electronic states and the structural flexibility of the VO_4^{3-} group, which allows for slight variations in bond lengths and angles, thereby influencing the energy levels involved in the transition. Additionally, the interaction between the vanadium–oxygen framework and the surrounding cations may further modulate the absorption properties, leading to variations in the absorption peak positions and intensities across different vanadate materials.[28–30] The DRS data were utilized to calculate the optical band gap of the materials. Fig. 2(b) showcases the band gap calculations derived from experimental data using the Kubelka–Munk formula.

The reflectance spectrum was converted to the absorption coefficient by employing the Kubelka–Munk function $F(R)$ as expressed in eqn (1).

$$F(R) = \frac{(1-R)^2}{2R} \quad (1)$$

where R denotes the observed reflectivity. The Tauc plot method was applied to determine the optical bandgap as given in eqn (2).

$$[F(R_\infty)h\nu]^2 = C(h\nu - E_g) \quad (2)$$

In this relation, E_g signifies the band gap energy, C is the proportionality constant, and $h\nu$ represents the photon energy. The band gap energy of a material can be determined from the intercept of the linear portion of the $[F(R_\infty)h\nu]^2$ *vs.* $h\nu$ plot, which represents the Tauc plot used for optical band gap estimation. In this study, the band gap values were found to be 3.73 eV for $Rb_3YV_2O_8$ and 3.89 eV for $Cs_3YV_2O_8$. The slight increase in the band gap upon substitution of Rb^+ with Cs^+ suggests that the replacement of alkali metal ions has only a minor influence on the optical properties of the present materials. This suggests that the variation in the ionic size and electronegativity between Rb^+ and Cs^+ has a minor influence on the electronic structure and optical absorption properties of the material. While the fundamental band structure remains largely intact, slight modifications in bond lengths, lattice parameters, and local electronic environments may contribute to subtle changes in the transition. These changes, though small, indicate that cation substitution can induce minor alterations

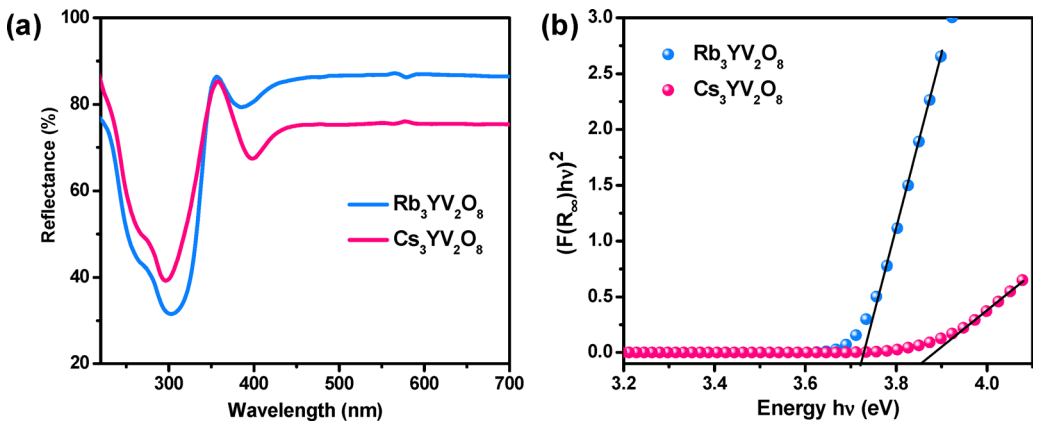

Fig. 2 (a) Diffuse reflectance spectra of $Rb_{3-x}Cs_xYV_2O_8$ (x = 0; $Rb_3YV_2O_8$ and x = 3; $Cs_3YV_2O_8$) and the corresponding (b) bandgap estimation using the Kubelka–Munk formula.

in the electronic density of states, potentially affecting charge carrier dynamics and optical transitions within the material.

3.3. Photoluminescence studies

To further analyze the dependency of optical properties on the variation of the alkali cation, we have recorded the photoluminescence excitation (PLE) and emission (PL) spectra of $Rb_{3-x}Cs_xYV_2O_8$ (x = 0; $Rb_3YV_2O_8$ and x = 3; $Cs_3YV_2O_8$) as shown in Fig. 3(a). The PLE spectrum of $Rb_3YV_2O_8$ materials was recorded keeping the emission wavelength fixed at 500 nm. The spectrum exhibits broad excitation bands in the 300–400 nm range peaking around 365 nm. The broad excitation band corresponds to charge-transfer transitions within the VO_4^{3-} tetrahedral units. These transitions originate from the electronic excitations between the oxygen ligands and the central vanadium atoms, specifically from the O 2p → V 3d states. The excitation spectra of $Cs_3YV_2O_8$ follow a similar pattern to $Rb_3YV_2O_8$ with a greater intensity.

To gain a detailed insight into broad excitation, the PLE spectrum of the $Cs_3YV_2O_8$ phosphors was deconvoluted using a Gaussian function (Fig. 3(b)). The deconvoluted peak positions of the PLE spectra are listed in Table 3. The PLE spectrum in the range of 300–400 nm has a peak at 360 nm and consists of two distinct bands at 335 nm (Ex_1) and 374 nm (Ex_2). The VO_4^{3-} tetrahedra possess a near tetrahedral (T_d) symmetry, in which the vanadium (V) ion is surrounded by four oxygen ligands. In this environment, the V 3d orbitals are split into two energy levels: the higher-energy t_2 orbitals and the lower-energy e orbitals. In a perfect tetrahedral (T_d) symmetry, the lower-energy e orbitals and the higher-energy t_2 orbitals are antibonding and experience stronger repulsion as they point toward the oxygen atoms. The ground state ($^1A_1$) of VO_4^{3-} is derived from the fully occupied e orbitals, while the singlet excited states $^1T_2$ and $^1T_1$ originate from the t_2 orbitals. The two bands at 335 nm (Ex_1) and 374 nm (Ex_2) correspond to the $^1A_1 \rightarrow {}^1T_2$ and $^1A_1 \rightarrow {}^1T_1$ transitions, respectively. These transitions are spin-allowed, resulting in strong absorption in the UV range.[31]

Table 3 Peak wavelength and energy of the PLE and PL bands from Gaussian deconvolution

	Band	Transition	Peak position (nm)	Energy (cm^{-1})	Energy (eV)
PLE	Ex_1	$^1A_1 \rightarrow {}^1T_2$	335	29 850.74	3.70
	Ex_2	$^1A_1 \rightarrow {}^1T_1$	374	26 737.96	3.31
PL	Em_1	$^3T_2 \rightarrow {}^1A_1$	476	21 008.40	2.60
	Em_2	$^3T_1 \rightarrow {}^1A_1$	537	18 621.97	2.30

The emission spectra of $Rb_{3-x}Cs_xYV_2O_8$ (x = 0; $Rb_3YV_2O_8$ and x = 3; $Cs_3YV_2O_8$), obtained at an excitation wavelength of 365 nm, span the visible range from 400 to 650 nm, with a maximum at approximately 500 nm. The substitution of Cs^+ for Rb^+ in $Rb_{3-x}Cs_xYV_2O_8$ significantly influences the local symmetry of the VO_4^{3-} units, altering their PL properties.[31]

To examine the variation in PL properties of the $Rb_{3-x}Cs_xYV_2O_8$ phosphors with increasing Cs^+ concentration, we have recorded the PL spectra of the $Rb_{3-x}Cs_xYV_2O_8$ (x = 0–3) phosphors as displayed in Fig. 4(a). The emission spectrum is characterized by a broad band from 400 to 650 nm. It can be noted that the emission spectra with different cationic ratios of Cs and Rb have a similar profile, but the luminescence intensity increases with increase in the cation substitution (x), with $Cs_3YV_2O_8$ having the maximum intensity. This indicates that the cation disorder has a great influence on the transition nature of VO_4 luminescence centers.[32]

To gain insight about the cation disorder, the PL spectrum was deconvoluted and the Gaussian-fitted PL spectrum was found to feature two emission bands at 476 nm (Em_1) and 537 nm (Em_2), as shown in Fig. 4(b). In addition to the singlet excited states as explained earlier, triplet states ($^3T_1$, $^3T_2$) also arise due to spin multiplicity, when an electron from the e orbital is promoted to the t_2 orbitals. The two emission bands at 476 nm (Em_1) and 537 nm (Em_2) correspond to the transitions $^3T_2 \rightarrow {}^1A_1$ and $^3T_1 \rightarrow {}^1A_1$ in VO_4^{3-}, respectively. Although

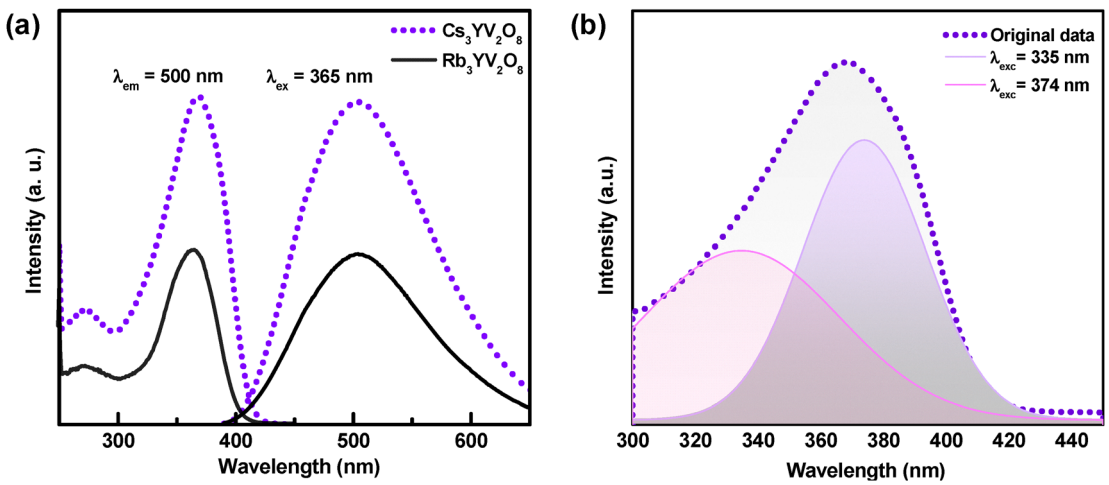

Fig. 3 (a) Photoluminescence excitation (PLE) and emission (PL) spectra of $Rb_{3-x}Cs_xYV_2O_8$ phosphors for x = 0: $Rb_3YV_2O_8$ and x = 3: $Cs_3YV_2O_8$. (b) Deconvolution of the excitation spectrum of $Cs_3YV_2O_8$.

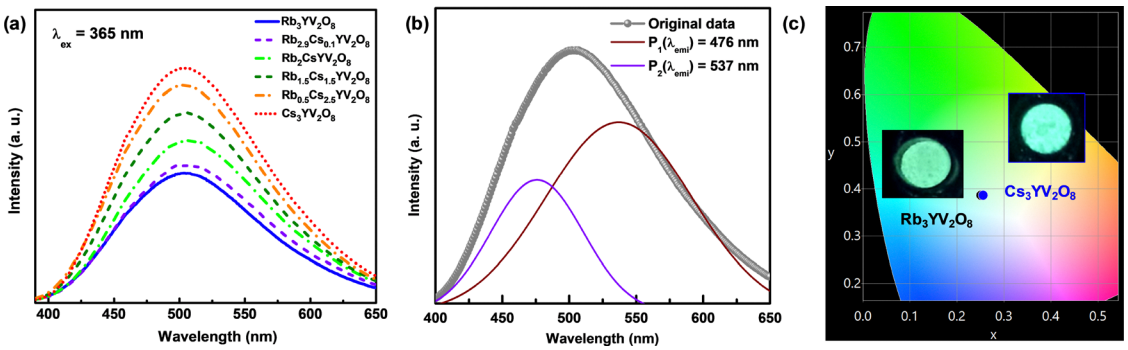

Fig. 4 (a) The PL spectra of $Rb_{3-x}Cs_xYV_2O_8$ with varying cesium concentrations from x = 0 to x = 3. (b) Deconvolution of the emission spectrum of $Cs_3YV_2O_8$. (c) The CIE diagram representing the emission color coordinates of $Rb_{3-x}Cs_xYV_2O_8$ (x = 0 and x = 3) with the corresponding PL images.

the spin selection rule generally forbids the excitation ($^1A_1 \rightarrow {}^1T_1$, $^1T_2$), intersystem crossing ($^1T_1$, $^1T_2 \rightarrow {}^3T_1$, $^3T_2$), and luminescence ($^3T_1$, $^3T_2 \rightarrow {}^1A_1$) processes in an ideal tetrahedral (T_d) symmetry, structural distortions in the VO_4^{3-} tetrahedron allow these transitions to occur. From XRD analysis, it is evident that Cs^+ (1.88 Å) after replacing Rb^+ (1.72 Å) expands the crystal lattice, causing VO_4 octahedra to interact strongly with each other, affecting the crystal field strength. This partially allows the forbidden transition from $^3T_1$, $^3T_2 \rightarrow {}^1A_1$. Similar findings by Nakajima *et al.* in AVO_3 (A = Rb, Cs) and $M_3V_2O_8$ (M = Mg, Zn) further support this effect, where increasing the cationic radius led to structural expansion and altered VO_4 tetrahedral interactions.[33] This change influenced the crystal field strength, partially relaxing selection rules and enabling otherwise forbidden transitions. As a result, the modified electronic environment enhanced the luminescence intensity, confirming the relationship between cation size and optical properties.[30] Meanwhile, there is not much shift in the emission color, as can be realized from the CIE diagram in Fig. 4(c), and the CIE coordinates of $Rb_3YV_2O_8$ and $Cs_3YV_2O_8$ are found to be (0.251, 0.386) and (0.256, 0.386). However, the PL images (inset in Fig. 4(c)) clearly indicated the superior emission intensity of $Cs_3YV_2O_8$ compared to that of $Rb_3YV_2O_8$.

As we explored the transition from Rb^+ to Cs^+ in $Rb_{3-x}Cs_xYV_2O_8$, we observed a fascinating enhancement in PL intensity. The Cs^+ substitution not only modified the electronic structure but also subtly altered the local crystal field environment. The result was a noticeable intensity variation in emission and an overall improvement in luminescence. Encouraged by this success, we wanted to push the boundaries further, to see whether we could deliberately disrupt the structural integrity and still enhance luminescence. Our structural analysis revealed that each [YO_6] octahedron shares six corners with alternating [VO_4] tetrahedra. Within these layers, the Cs^+ cations were strategically positioned, providing charge balance and stability.

By introducing Bi^{3+} into the system, we tried to further manipulate the optical properties. For this purpose, we synthesized a series of $Cs_3Bi_yY_{1-y}V_2O_8$ (y = 0 to 1) and conducted a detailed PL analysis. Fig. 5(a) and (b) present the PLE and PL spectra of $Cs_3Bi_yY_{1-y}V_2O_8$ (y = 0 to 1), respectively. The PLE spectra were recorded at a fixed emission wavelength of 500 nm, while the PL spectra were measured by exciting the samples at 365 nm. These spectra illustrate the excitation–emission behaviour and the impact of Bi^{3+} substitution on luminescence properties. The results were remarkably impressive. As Bi^{3+} was progressively incorporated, the PL intensity saw a significant increase. This observation suggested that the introduction of a cation had a passive yet profound influence on the electronic environment of the host lattice.

Moreover, we observed a redshift in the normalized photoluminescence (PL) spectra with increasing Bi content, as illustrated in Fig. 5(c). In the $Cs_3Bi_yY_{1-y}V_2O_8$ system, the observed red-shift of the PL emission upon Bi^{3+} incorporation is primarily attributed to structural modifications in the host lattice. Although Bi^{3+} and Y^{3+} have similar ionic radii, the introduction of the heavier Bi^{3+} ions alters the local bonding environment and lattice dynamics in several subtle but significant ways. Partial substitution of Y^{3+} by Bi^{3+}results in a slight expansion of the unit cell and perturbation of the local symmetry around the VO_4 tetrahedra. This modifies the V–O bond lengths and O–V–O bond angles, slightly lowering the crystal field strength experienced by the vanadate units. This structural perturbation affects the splitting of the vanadate tetrahedral orbitals, leading to a reduction in the energy difference between the excited and ground states of the VO_4^{3-} groups. This manifests as a red-shift in the emission peak without the involvement of additional electronic transitions from Bi^{3+}. Moreover, the heavier Bi^{3+} ions introduce minor local strain and increase polarizability around the vanadate units, which can enhance electron–phonon coupling. This not only broadens the emission band but also contributes to a lower-energy recombination pathway, further shifting the emission to longer wavelengths.[30–35] The CIE diagram, shown in Fig. 5(d), also supports the red shift of the emission color from bluish green to greenish yellow with increasing the Bi^{3+} to Y^{3+} ion substitution. The CIE coordinates of $Cs_3YV_2O_8$ (0.251, 0.386) are drastically shifted to (0.364, 0.465) for $Cs_3BiV_2O_8$, which is also clearly visible in the PL images of these two samples (Fig. 5(e)). Meanwhile, the most red-shifted $Cs_3BiV_2O_8$ phosphor exhibits a broader emission bandwidth, and its emission intensity is comparable to that of the commercial blue phosphor BAM:Eu^{2+}, as shown in Fig. 5(f).

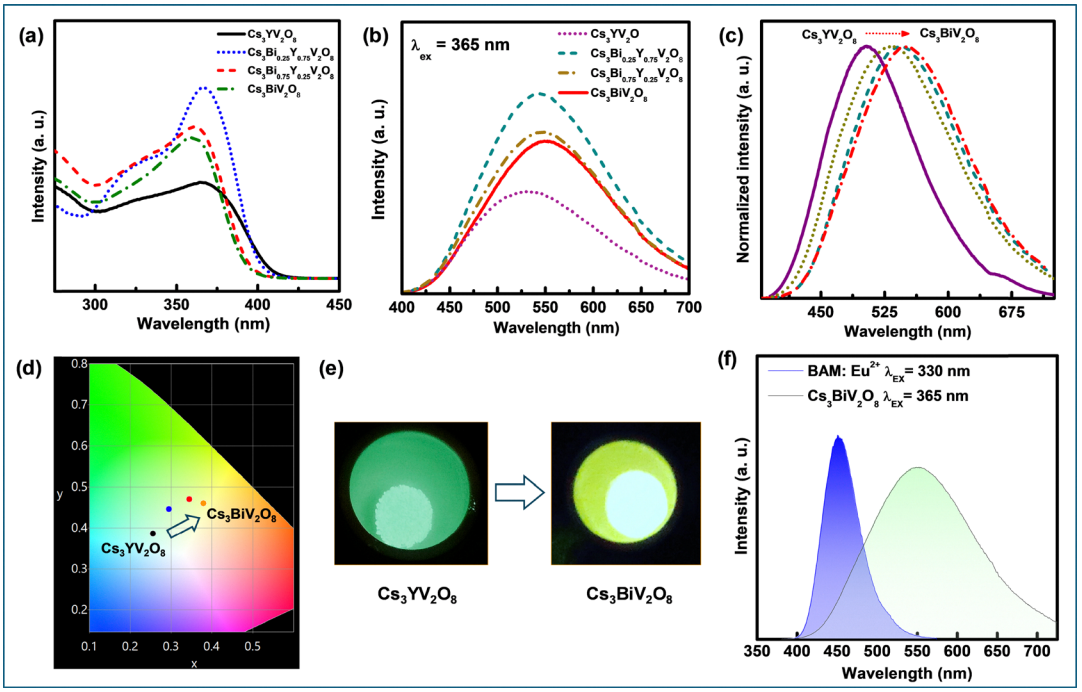

Fig. 5 (a) The PLE spectra of $Cs_3Bi_yY_{1-y}V_2O_8$ (y = 0 to 1) at $\lambda_{emi} \approx 500$ nm. (b) The PL spectra of $Cs_3Bi_yY_{1-y}V_2O_8$ (y = 0 to 1) at $\lambda_{exc} \approx 365$ nm. (c) The normalized PL spectra of $Cs_3Bi_yY_{1-y}V_2O_8$ (y = 0 to 1). (d) The CIE diagram representing the emission color coordinates of $Cs_3YV_2O_8$ and $Cs_3BiV_2O_8$ with the corresponding PL images. (e) Digitized images showing the color evolution from cyan-green to green with Bi addition in the $Cs_3YV_2O_8$ host. (f) Comparison of emission band broadening in the present phosphor system relative to the commercial BAM:Eu^{2+} standard.

This phenomenon further reinforces the idea that Bi^{3+} acts as an active luminescence modifier rather than merely a passive dopant. By systematically varying the Bi^{3+} concentration, we effectively tuned the emission properties of the phosphor, demonstrating a controlled approach to adjusting the luminescence behavior through targeted cationic substitution. What initially began as a simple substitution process evolved into a precise strategy for engineering emission color, highlighting the potential of Bi^{3+} incorporation as a versatile tool for tailoring optical properties in vanadate-based phosphors. This result underscores the critical role of crystal field effects and electronic interactions in designing next-generation phosphor materials with tunable emission characteristics for advanced lighting applications.

To assess the luminescence performance of the synthesized phosphors further, the luminescence decay behavior of three representative samples was also investigated. The corresponding luminescence decay curves of $Rb_3YV_2O_8$, $Cs_3YV_2O_8$, and $Cs_3Bi_{0.25}Y_{0.75}V_2O_8$, as shown in Fig. 6, were well fitted by a single-exponential function, suggesting the presence of a uniform emission center in all samples. The average lifetimes were found to increase slightly from 643 μs for $Rb_3YV_2O_8$ to 651 μs for $Cs_3YV_2O_8$, while $Cs_3Bi_{0.25}Y_{0.75}V_2O_8$ exhibited an intermediate lifetime of 648 μs. These results confirmed a decrease in non-radiative losses of excitation energy with the substitution of larger cations. Furthermore, to evaluate their practical applicability, three white light-emitting diodes (WLEDs) were fabricated using the synthesized phosphor powders as conversion layers.

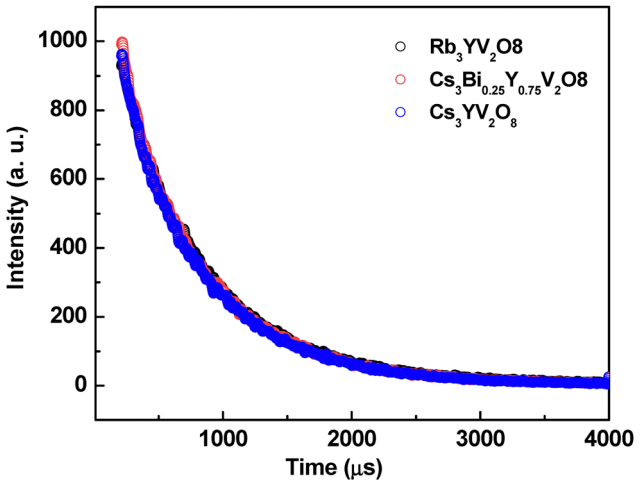

Fig. 6 Emission decay curves of $Rb_3YV_2O_8$, $Cs_3Bi_{0.25}Y_{0.75}V_2O_8$ and $Cs_3YV_2O_8$.

3.4. Analysis of temperature-dependent photoluminescence

The thermal stability of a phosphor is a crucial parameter in determining its suitability for light-emitting diode (LED) applications, as it directly influences emission performance under elevated operating temperatures. To assess the thermal behavior of the synthesized phosphor, temperature-dependent photoluminescence (PL) spectra of $Cs_3Bi_{0.25}Y_{0.75}V_2O_8$ were recorded over a temperature range of 303 K to 448 K using an excitation wavelength of 365 nm. Fig. 7(a) provides a three-dimensional representation of the spectra, where red regions

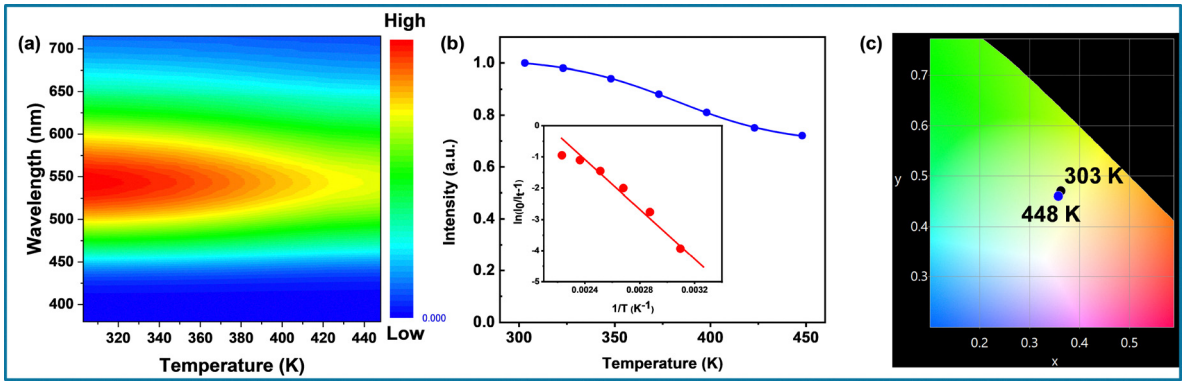

Fig. 7 (a) Temperature-dependent PL of $Cs_3Bi_{0.25}Y_{0.75}V_2O_8$. (b) Thermal quenching behaviour of $Cs_3Bi_{0.25}Y_{0.75}V_2O_8$ (inset shows the Arrhenius plot for the estimation of E_a). (c) The CIE diagram showing the $Cs_3Bi_{0.25}Y_{0.75}V_2O_8$ phosphor's emission color shift due to the increase in temperature from 303 K to 448 K.

indicate high emission intensity, while blue regions correspond to lower intensity. The results demonstrate a decline in PL emission intensity with increasing temperature, which can be attributed to the thermal quenching phenomenon.[34,35] This phenomenon, widely observed in phosphor materials, occurs due to enhanced non-radiative relaxation processes at elevated temperatures, leading to energy dissipation and a subsequent reduction in luminescence efficiency. Fig. 7(b) depicts the variation in normalized photoluminescence (PL) intensity as a function of temperature, providing a comprehensive evaluation of the thermal stability of the synthesized phosphor. The results indicate a substantial decrease in PL intensity, with a reduction of 75.05% recorded at 423 K. This decline underscores the influence of elevated temperatures on the luminescence properties of the material. Notably, the synthesized phosphor demonstrates superior thermal stability compared to previously reported VO_4^{3-}-activated vanadate and Bi^{3+}-doped oxide phosphor systems, as summarized in Table 4. The enhanced performance suggests that the material retains a higher emission intensity under high-temperature conditions, making it a promising candidate for high-power LED applications. As the temperature increases, lattice vibrations become more pronounced, leading to enhanced generation of thermally activated phonons. These phonons facilitate non-radiative transitions by providing electrons with the necessary energy to overcome the energy barrier (ΔE) and return to the ground state without photon emission. This process results in substantial energy dissipation and a marked reduction in the phosphor's luminous intensity.[35,36] Accurately assessing this energy barrier is therefore crucial for understanding and mitigating the thermal quenching effects.

In the present study, the Arrhenius equation was employed to systematically investigate the relationship between photoluminescence (PL) emission and temperature, providing insights into the extent of thermal quenching. This approach allowed for the calculation of the activation energy (E_a), which serves as a key parameter in evaluating the thermal stability of the phosphor. A higher E_a value indicates greater resistance to thermally induced non-radiative losses, signifying enhanced structural stability of the host matrix. The following equation was employed to determine E_a.[37]

$$\ln\left[\frac{I_0}{I_t} - 1\right] = \ln[c] - \frac{E_a}{kT} \quad (3)$$

Table 4 Comparisons of the photoluminescence properties (λ_{ex}, λ_{em}, CRI, CCT) and thermal properties of VO_4-activated vanadate and Bi^{3+}-doped phosphors

Phosphor	λ_{ex} (nm)	λ_{em} (nm)	PL intensity (@423 K)	E_a (eV)	CRI (Ra)	CCT (K)	Ref.
$Mg_3(VO_4)_2$	340	550	26%	—	83	5500	38
$Ba_3(VO_4)_2$	340	490	19%	—	84	5349	38
$RbLuV_2O_8$	362	500	51%	0.264	93.5	4946	39
$Rb_3YV_2O_8$	362	500	48%	0.266	91.9	5095	39
$KCa_2Mg_2V_3O_{12}$	346	540	21%	0.366	<80	>4500	40
$RbVO_3$	360	520	62%	0.288	—	—	41
$Ca_5Mg_4(VO_4)_6$	346	544	62%	—	82.5	5231	42
$Zn_3V_2O_8$	350	550	51%	—	—	—	43
$CaLaGaO_4$:5%Bi^{3+}	361	448	86%	0.3	—	5426	44
BGBO:0.4% Bi^{3+}	320	560	20%	—	79.1	4331	45
$BaYb_{4.2}P_{0.8}$:Bi^{3+}	340	530	50%	0.277	90.1	4509	46
$Lu_2SrAl_4SiO_{12}$:0.08 Bi^{3+}	330	466	57.2%	0.22	88	5723	47
$CaLuGaO_4$:0.004 Bi^{3+}	335	427	91.8%	0.289	>90	<6000	48
NLSNO:10 mol%Bi^{3+}	370	625	76%	—	92	—	49
$Ba_3SbAl_3Ge_2O_{14}$:0.1 Bi^{3+}	365	560	76%	—	91.5	4229	50
$Ca_2LuZrScAl_2GeO_{12}$:0.14 Bi^{3+}	467	365	80%	0.21	98.5	4455	51
$Ba_3Lu_2B_6O_{15}$:0.1 Bi^{3+}	365	417	71%	0.215	82.6	4495	52
$Cs_3Bi_{0.25}Y_{0.75}V_2O_8$	365	543	85.7%	0.32	79	4882	**This work**

here, k represents Boltzmann's constant, E_a is the activation energy, I_0 is the initial emission intensity, and I_t is the emission intensity at temperature T. By analyzing the slope of the linearly fitted curve, the E_a for the system was determined to be 0.32 eV (inset in Fig. 7(b)). This value represents the minimum energy required to activate the non-radiative relaxation processes, which contribute to thermal quenching. In comparison to previously reported vanadate phosphors, as summarized in Table 4, the synthesized phosphor exhibits a higher E_a, indicating greater resistance to thermally induced non-radiative losses. This enhanced E_a value correlates with improved thermal stability, suggesting that the material maintains its luminescence efficiency more effectively at elevated temperatures and highlighting its potential for application in high-power LED devices, where performance retention under high-temperature operating conditions is crucial. Another crucial fact to note is that the CIE color coordinate remained almost invariant due to the temperature variations, as observed in Fig. 7(c). These findings underscore the advantages of the developed phosphor in mitigating the thermal quenching effects, making it a promising candidate for next-generation optoelectronic applications.

3.5. Phosphor-converted white light emitting diode and electroluminescence studies

First, 99% silicon A was mixed with 1% silicon B, and the resulting powder sample was combined with a precursor in an appropriate ratio. The mixture was then injected onto the surface of a UV LED chip emitting at 365 nm and placed in a vacuum oven at 90 °C for 6 hours. The vacuum environment helped prevent air bubbles and ensured a smooth phosphor layer on the chip, leading to the successful fabrication of WLEDs. The electroluminescence (EL) spectra and the corresponding luminescence images of $Rb_3YV_2O_8$, $Cs_3YV_2O_8$ and $Cs_3Bi_{0.25}Y_{0.75}V_2O_8$ are presented in Fig. 8(a). The spectra showed a significant improvement in EL intensity for $Cs_3YV_2O_8$ compared to $Rb_3YV_2O_8$. The CIE chromaticity coordinates, correlated color temperature (CCT), and color rendering index (CRI) were calculated using a color calculator software as mentioned in Table 5.

The WLEDs based on $Rb_3YV_2O_8$ exhibited a CCT of 6557 K, a CRI of 74 and CIE coordinates of (0.28, 0.39), while those with $Cs_3YV_2O_8$ showed a CCT of 6111 K, a CRI of 78 and CIE coordinates of (0.29, 0.40). Although the CCT values were similar, our goal was to enhance red coverage. Notably, after introducing Bi into the host, the $Cs_3Bi_{0.25}Y_{0.75}V_2O_8$ phosphor produced a bright warm white emission with CIE coordinates of (0.34, 0.40). The phosphor achieved a CCT of 4887 K, while the CRI slightly improved to 79. As shown in the CIE coordinate diagram in Fig. 8(b), successful tuning of the emission from cool white (6557 K) to more human-centric white (4887 K) makes the phosphor well-suited for reading room lighting.

Although the composition $Cs_3Bi_{0.25}Y_{0.75}V_2O_8$ exhibits a higher emission intensity, the phosphor of primary interest in this study is $Cs_3BiV_2O_8$, for two key reasons. First, it is a rare-earth-free composition, which is advantageous in terms of cost and sustainability. Second, as indicated in Fig. 9, its emission lies more prominently in the yellowish region of the visible spectrum. The EL spectra of a pc-LED device fabricated using this phosphor in combination with a 365 nm UV LED demonstrate effective

Table 5 CIE Coordinates, CCT and CRI of the WLEDs fabricated with synthesized materials

Sample	CIE coordinates	CCT (K)	CRI
$Rb_3YV_2O_8$	(0.28, 0.39)	6557	74
$Cs_3YV_2O_8$	(0.29, 0.40)	6111	78
$Cs_3Bi_{0.25}Y_{0.75}V_2O_8$	(0.34, 0.40)	4887	79

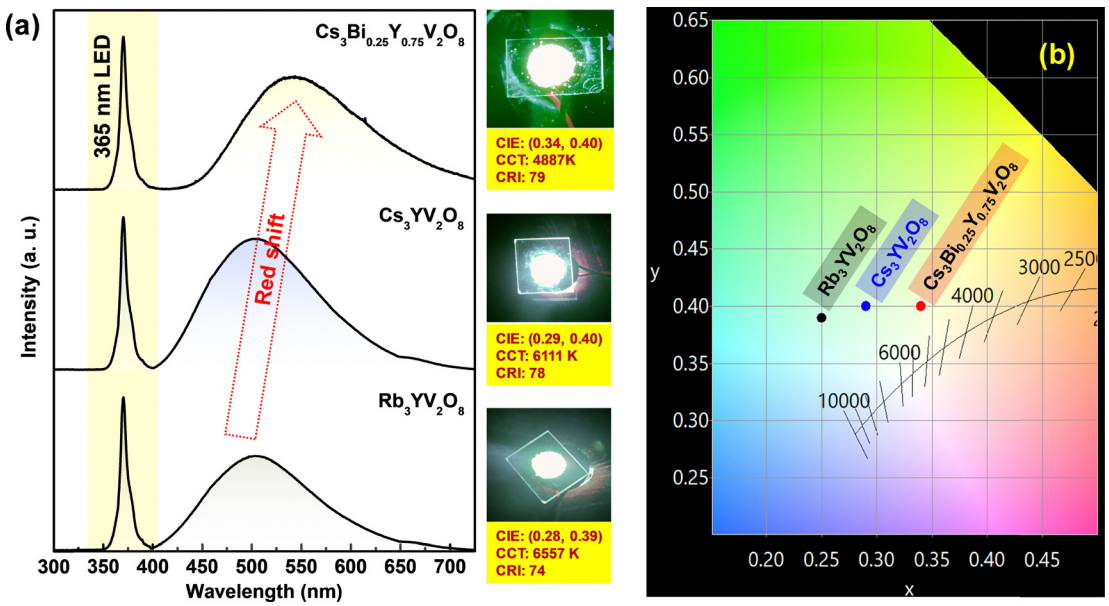

Fig. 8 (a) The electroluminescence spectra, corresponding color coordinates, and digital LED images of $Cs_3Bi_{0.25}Y_{0.75}V_2O_8$, $Cs_3YV_2O_8$, and $Rb_3YV_2O_8$. (b) The corresponding CIE coordinates for the respective phosphors.

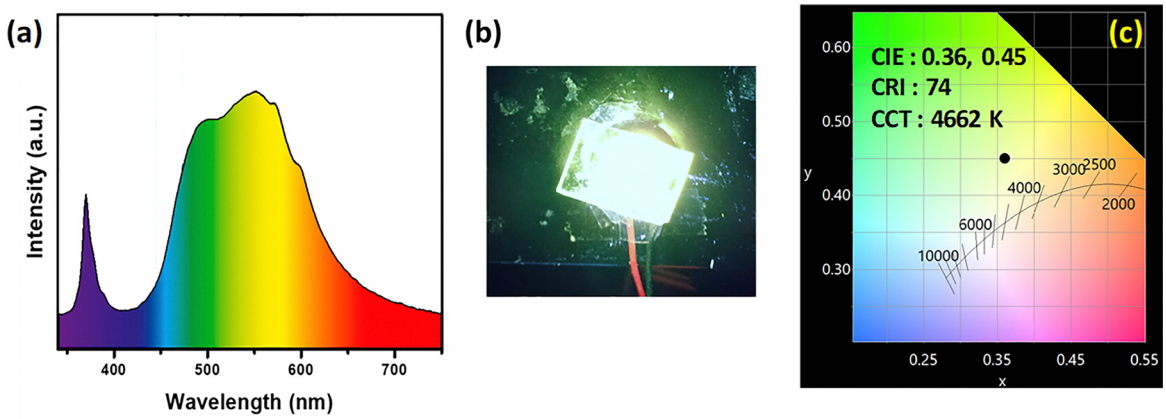

Fig. 9 (a) The electroluminescence spectra and (b) digital LED images of the pc LED fabricated with $Cs_3BiV_2O_8$. (c) The corresponding CIE coordinates for the respective phosphors.

color conversion and yield a bright yellowish-white emission, as shown in Fig. 9(a) and (b), respectively. The calculated CIE coordinates are (0.36, 0.45), with a CRI of approximately 74 and a correlated color temperature (CCT) of around 4662 K, as shown in Fig. 9(c). Table 4 summarizes the results of the present material and those of previously reported Bi^{3+}-activated materials. These results underscore the potential of this optimized phosphor as a single-component material for UV-chip-based phosphor-converted WLEDs, making it a promising candidate for indoor lighting applications. In our forthcoming work, we plan to extend this investigation by systematically modifying the host composition and dopant concentration to achieve more effective cyan and red gap filling. These efforts will include quantitative evaluation of spectral overlap integrals and luminescence enhancement parameters to establish precise correlations between structural tuning and emission broadening.

4. Conclusions

In this study, a series of $Rb_{3-x}Cs_xYV_2O_8$ phosphors were successfully synthesized, exhibiting a broad emission spectrum spanning 400–650 nm, with a peak centered around 500 nm under 365 nm near-ultraviolet excitation. Rietveld refinement confirmed that the synthesized luminescence emitters crystallize in the trigonal structure with a space group of $P\bar{3}m1$. By engineering an O 2p → V 3d energy transfer mechanism, tunable emission from cyan-green to yellowish white was achieved in $Rb_{3-x}Cs_xYV_2O_8$ through Bi^{3+} incorporation. This emission shift was attributed to local crystal field modifications induced by Bi^{3+} ions, which altered the ligand environment and consequently influenced the electronic structure. Temperature-dependent photoluminescence analysis revealed that the phosphor retained 75.05% of its initial emission intensity at 423 K, with an activation energy of 0.32 eV, demonstrating excellent thermal stability. To assess the practical viability of these phosphors, they were integrated into white light-emitting diodes (WLEDs). The resulting devices exhibited distinct emission characteristics: $Rb_3YV_2O_8$-based LEDs produced cool white light (CCT ≈ 6557 K, CRI ≈ 74, CIE ≈ 0.25, 0.39), while $Cs_3Bi_{0.25}Y_{0.75}V_2O_8$-based LEDs emitted a warmer white light (CCT ≈ 4887 K, CRI ≈ 79, CIE ≈ 0.32, 0.40). By systematically investigating structural modifications, optical tunability, and practical implementation, this study underscores the effectiveness of rational design strategies in optimizing phosphor performance for next-generation lighting technologies. Moreover, the insights gained into the effects of cation substitution and Bi^{3+} doping on luminescence provide a foundation for the advancement of high-performance phosphors, facilitating the development of efficient, natural-sunlight-like white light sources.

Conflicts of interest

There are no conflicts to declare.

Data availability

All the data that support this research are included within the article.

Acknowledgements

This research was financially supported by the Council of Scientific & Industrial Research (CSIR), Govt. of India, through the Advanced Materials Mission program under the 4M theme (Project no. HCP0030). The authors S. S., M. B. and J. D. extend their heartfelt gratitude to Shiv Nadar University, Chennai, for supporting this research through a seed fund grant (No. SNU/IFFP/April2023/1-2/01). The research was also supported partially by the Anusandhan National Research Foundation (ANRF) (Project no. CRG/2023/008765).

References

1 A. Zhou and Y. Pan, Effects of indoor lighting environments on paper reading efficiency and brain fatigue: an experimental study, *Front. Built Environ.*, 2023, **9**, 1303028, DOI: 10.3389/fbuil.2023.1303028.

2 M. Sánchez-Lacambra, E. Orduna-Hospital, M. Arcas-Carbonell and A. Sánchez-Cano, Effects of Light on Visual Function, Alertness, and Cognitive Performance: A Computerized Test Assessment, *Appli. Sci.*, 2024, **14**, 6424, DOI: 10.3390/app14156424.
3 Q. Huang, Exploring the impact of indoor lighting environment on learning and work efficiency, *Advances in Operation Research and Production Management*, 2024, **2**, 50–55, DOI: 10.54254/3029-0880/2/2024017.
4 Y. C. Li, L. B. Chang, H. J. Chen, C. Y. Yen, K. W. Pan, B. R. Huang, W. Y. Kuo, L. Chow, D. Zhou and E. Popko, Phosphor-free ingan white light emitting diodes using flip-chip technology, *Materials*, 2017, **10**, 432, DOI: 10.3390/ma10040432.
5 H. Zeng, T. Chen, Y. Guo and X. Wu, Yttrium aluminum garnet fluorescent conversion films for solid-state lighting: interface reaction synthesis strategy and modulation of warm white light, *Dalton Trans.*, 2025, **54**, 3930–3938, DOI: 10.1039/D4DT03316G.
6 P. T. That and P. X. Le, The qualities of dyed YAG:Ce3 + @SiO2 for WLEDs via energy conversion, *Bull. Electr. Eng. Inform.*, 2022, **11**, 2587–2594, DOI: 10.11591/eei.v11i5.4064.
7 J. Cho, J. H. Park, J. K. Kim and E. F. Schubert, White light-emitting diodes: History, progress, and future, *Laser Photon. Rev.*, 2017, **11**, 1600147, DOI: 10.1002/lpor.201600147.
8 J. Y. Tsao, M. H. Crawford, M. E. Coltrin, A. J. Fischer, D. D. Koleske, G. S. Subramania, G. T. Wang, J. J. Wierer and R. F. Karlicek Jr., Toward Smart and Ultra-efficient Solid-State Lighting, *Adv. Opt. Mater.*, 2014, **2**, 809–836, DOI: 10.1002/adom.201400131.
9 S. E. Brinkley, N. Pfaff, K. A. Denault, Z. Zhang, H. T. (Bert) Hintzen, R. Seshadri, S. Nakamura and S. P. DenBaars, Robust thermal performance of Sr2Si5N8:Eu2 +: An efficient red emitting phosphor for light emitting diode based white lighting, *Appl. Phys. Lett.*, 2011, **99**, 241106, DOI: 10.1063/1.3666785.
10 N. H. K. Nhan, T. H. Q. Minh, T. N. Nguyen and M. Voznak, Bi-layers Red-emitting Sr2Si5N8:Eu2+ Phosphor and Yellow-emitting YAG:Ce Phosphor: A New Approach for Improving the Color Rendering Index of the Remote Phosphor Packaging WLEDs, *Curr. Opt. Photon.*, 2017, **1**, 613–617.
11 H. Nersisyan, H. Il Won and C. W. Won, Highly effective synthesis and photoluminescence of Sr2Si5N8:Eu2+ red-emitting phosphor for LEDs, *Chem. Commun.*, 2011, **47**, 11897–11899, DOI: 10.1039/C1CC15427C.
12 T. Kang, S. Lee, T. Kim and J. Kim, Efficient Luminescence of Sr2Si5N8:Eu2+ nanophosphor and its film applications to LED and Solar cell as a downconverter, *Sci. Rep.*, 2020, **10**, 1475, DOI: 10.1038/s41598-020-58469-7.
13 T. Wang, K. Li, B. Yao, Y. Chen, H. Zhan, Z. Xie, G. Xie, X. Yi and Y. Cheng, Rigidity and Polymerization Amplified Red Thermally Activated Delayed Fluorescence Polymers for Constructing Red and Single-Emissive-Layer White OLEDs, *Adv. Funct. Mater.*, 2020, **30**, 2002493, DOI: 10.1002/adfm.202002493.
14 J. M. Collier, A. Wilkerson, D. Durmus and E. Rodriguez-Feo Bermudez, Studying Response to Light in Offices: A Literature Review and Pilot Study, *Buildings*, 2023, **13**, 471, DOI: 10.3390/buildings13020471.
15 S. T. Peeters, K. C. H. J. Smolders, I. M. L. C. Vogels and Y. A. W. de Kort, Less is more? Effects of more vs. less electric light on alertness, mood, sleep and appraisals of light in an operational office, *J. Environ. Psychol.*, 2021, **74**, 101583, DOI: 10.1016/j.jenvp.2021.101583.
16 Y. Huang, Y. Nakai, T. Tsuboi and H. J. Seo, The new red-emitting phosphor of oxyfluoride Ca2RF4PO4:Eu3+ (R = Gd, Y) for solid state lighting applications, *Opt. Express*, 2011, **19**, 6303–6311, DOI: 10.1364/OE.19.006303.
17 K. Deng, T. Gong, Y. Chen, C. Duan and M. Yin, Efficient red-emitting phosphor for near-ultraviolet-based solid-state lighting, *Opt. Lett.*, 2011, **36**, 4470–4472, DOI: 10.1364/OL.36.004470.
18 S. E. Brinkley, N. Pfaff, K. A. Denault, Z. Zhang, H. T. Hintzen, R. Seshadri, S. Nakamura and S. P. Denbaars, Robust thermal performance of Sr 2Si 5N 8:Eu 2 +: An efficient red emitting phosphor for light emitting diode based white lighting, *Appl. Phys. Lett.*, 2011, **99**, 241106, DOI: 10.1063/1.3666785.
19 Z. Li, T. Seto and Y. Wang, Enhanced Thermal Stability of Red-Emitting Sr2Si5N8:Eu2+ Phosphors from Triggered Applicable Trap Level via Rare Earth Ions Co-Doping, *Adv. Funct. Mater.*, 2024, **34**, 2309086, DOI: 10.1002/adfm.202309086.
20 X. Yang, X.-J. Xing, Y.-F. Liu, C.-H. Mu, H. Van Bui, Z.-W. Zhang, S. Agathopoulos, X. Xu and L.-J. Yin, A new thermal degradation mechanism of red Sr2Si5N8:Eu phosphor: From the view of microstructural evolution, *Opt. Mater.*, 2021, **121**, 111506, DOI: 10.1016/j.optmat.2021.111506.
21 M. Kim, M. Kobayashi, H. Kato and M. Kakihana, Enhancement of luminescence properties of a KSrPO4:Eu2+ phosphor prepared using a solution method with a water-soluble phosphate oligomer, *J. Mater. Chem. C*, 2013, **1**, 5741–5746, DOI: 10.1039/C3TC31121J.
22 S. Li, Q. Zhu, L. Wang, D. Tang, Y. Cho, X. Liu, N. Hirosaki, T. Nishimura, T. Sekiguchi, Z. Huang and R.-J. Xie, CaAlSiN3:Eu2+ translucent ceramic: a promising robust and efficient red color converter for solid state laser displays and lighting, *J. Mater. Chem. C*, 2016, **4**, 8197–8205, DOI: 10.1039/C6TC02518H.
23 I. Jaadane, P. Boulenguez, S. Chahory, S. Carré, M. Savoldelli, L. Jonet, F. Behar-Cohen, C. Martinsons and A. Torriglia, Retinal damage induced by commercial light emitting diodes (LEDs), *Free Radic. Biol. Med.*, 2015, **84**, 373–384, DOI: 10.1016/j.freeradbiomed.2015.03.034.
24 P. Dang, D. Liu, Y. Wei, G. Li, H. Lian, M. Shang and J. Lin, Highly Efficient Cyan-Green Emission in Self-Activated Rb3RV2O8 (R = Y, Lu) Vanadate Phosphors for Full-Spectrum White Light-Emitting Diodes (LEDs), *Inorg. Chem.*, 2020, **59**, 6026–6038, DOI: 10.1021/acs.inorgchem.0c00015.
25 R. D. Shannon, Revised Effective Ionic Radii and Systematic Studies of Interatomic Distances in Halides and Chalcogenides, *Acta Cryst.*, 1976, **32**, 751–767, DOI: 10.1107/S0567739476001551.
26 M. Paul Brian, Bracelets and pinwheels: A topological-geometrical approach to the calcium orthosilicate and alkali sulfate structures, *Am. Mineral.*, 1973, **58**, 32–42.
27 F. C. Hawthorne, S. V. Krivovichev and P. C. Burns, in The crystal chemistry of sulfate minerals, *Sulfate Minerals: Crystallography,*

Geochemistry, and Environmental Significance, Walter de Gruyter GmbH, 2019, pp. 1–112, DOI: 10.2138/rmg.2000.40.1.

28 T. Hasegawa, Y. Abe, A. Koizumi, T. Ueda, K. Toda and M. Sato, Bluish-White Luminescence in Rare-Earth-Free Vanadate Garnet Phosphors: Structural Characterization of LiCa3MV3O12 (M = Zn and Mg), *Inorg. Chem.*, 2018, **57**, 857–866, DOI: 10.1021/acs.inorgchem.7b02820.

29 T. Nakajima, M. Isobe, T. Tsuchiya, Y. Ueda and T. Manabe, Correlation between luminescence quantum efficiency and structural properties of vanadate phosphors with chained, dimerized, and isolated VO4 tetrahedra, *J. Phys. Chem. C*, 2010, **114**, 5160–5167, DOI: 10.1021/jp910884c.

30 T. Nakajima, M. Isobe, T. Tsuchiya, Y. Ueda and T. Manabe, Correlation between luminescence quantum efficiency and structural properties of vanadate phosphors with chained, dimerized, and isolated VO 4 tetrahedra, *J. Phys. Chem. C*, 2010, **114**, 5160–5167, DOI: 10.1021/jp910884c.

31 H. Ronde and G. Blasse, The nature of the electronic transitions of the vanadate group, *J. Inorg. Nucl. Chem.*, 1978, **40**, 215–219, DOI: 10.1016/0022-1902(78)80113-4.

32 A. K. Dehury, R. Kainda and Y. S. Chaudhary, Mechanistic Insight into the Defect-Engineered White Light Emission from the Single-Phase Orthovanadate Phosphor Synthesized by a Facile Rapid Microwave-Assisted Synthesis, *Inorg. Chem.*, 2023, **62**, 17163–17181, DOI: 10.1021/acs.inorgchem.3c02156.

33 A. L. Heyes, On the design of phosphors for high-temperature thermometry, *J. Lumin.*, 2009, **129**, 1598–1601, DOI: 10.1016/j.jlumin.2009.03.029.

34 T. Qian, B. Fan, H. Wang and S. Zhu, Structure and luminescence properties of Zn3V2O8 yellow phosphor for white light emitting diodes, *Chem. Phys. Lett.*, 2019, **715**, 34–39, DOI: 10.1016/j.cplett.2018.11.022.

35 Z. Liu, Y. Dong, M. Fu and C. Wang, Highly efficient rare-earth free vanadate phosphors for WLEDs, *Dalton Trans.*, 2023, **52**, 16819–16828, DOI: 10.1039/D3DT03138A.

36 Q. Lv, C. Wang, S. Chen, H. Zheng, E. Dong and G. Zhu, Ultrasensitive Pressure-Induced Optical Materials: Europium-Doped Hafnium Silicates with a Khibinskite Structure for Optical Pressure Sensors and WLEDs, *Inorg. Chem.*, 2022, **61**, 3212–3222, DOI: 10.1021/acs.inorgchem.1c03674.

37 T. Qian, B. Fan, H. Wang and S. Zhu, Structure and luminescence properties of Zn3V2O8 yellow phosphor for white light emitting diodes, *Chem. Phys. Lett.*, 2019, **715**, 34–39, DOI: 10.1016/j.cplett.2018.11.022.

38 N. He, W. S. Kim, S. M. Chang and Z. Li, A special section on applications of nanotechnology in biomaterials and bioassays, *J. Nanosci. Nanotechnol.*, 2016, **16**, 12069–12070, DOI: 10.1166/jnn.2016.12937.

39 P. Dang, D. Liu, Y. Wei, G. Li, H. Lian, M. Shang and J. Lin, Highly Efficient Cyan-Green Emission in Self-Activated Rb3RV2O8 (R = Y, Lu) Vanadate Phosphors for Full-Spectrum White Light-Emitting Diodes (LEDs), *Inorg. Chem.*, 2020, **59**, 6026–6038, DOI: 10.1021/acs.inorgchem.0c00015.

40 X. Huang, S. Wang, S. Rtimi and B. Devakumar, KCa2Mg2V3O12: A novel efficient rare-earth-free self-activated yellow-emitting phosphor, *J. Photochem. Photobiol. A*, 2020, **401**, 112765, DOI: 10.1016/j.jphotochem.2020.112765.

41 S. W. Kim, T. Hasegawa, M. Muto, A. Toda, T. Kaneko, K. Sugimoto, K. Uematsu, T. Ishigaki, K. Toda, M. Sato, J. Koide, M. Toda and Y. Kudo, Improvement of luminescence properties of rubidium vanadate, RbVO3, phosphors by erbium doping in the crystal lattice, *New J. Chem.*, 2017, **41**, 4788–4792, DOI: 10.1039/C6NJ03823A.

42 Z. Liu, Y. Dong, M. Fu and C. Wang, Highly efficient rare-earth free vanadate phosphors for WLEDs, *Dalton Trans.*, 2023, **52**, 16819–16828, DOI: 10.1039/d3dt03138a.

43 S. Shisina, P. K. Thejus, K. G. Nishanth and S. Das, Multifaceted insight into the cation-disordered self-activated luminescence of Zn3V2O8 compositions for lighting and pigment applications, *J. Mater. Chem. C*, 2024, **12**, 4037–4053, DOI: 10.1039/D3TC04503J.

44 N. Navya, B. R. R. Krushna, S. C. Sharma, D. Mohapatra, S. Begum, Aishwarya, G. B. Protyusha, K. Manjunatha, S. Y. Wu, R. Arunakumar and H. Nagabhushana, Broadband blue-emitting CaLaGaO4:Bi3+ phosphors with persistent afterglow for High-CRI w-LEDs and advanced anti-counterfeiting applications, *Ceram. Int.*, 2025, **51**, 39558–39575, DOI: 10.1016/j.ceramint.2025.06.191.

45 Y. Yang, M. He, J. Yao, X. Zhu, C. Wang, J. Yang, F. Lin, J. Wang and R. Wang, Bi3 + -activated high-efficiency full-spectrum WLEDs with broadband yellow-green emission Ba2Gd5-B5O17:Bi3+ phosphor, *Ceram. Int.*, 2025, **51**, 27023–27031, DOI: 10.1016/j.ceramint.2025.03.383.

46 X. Liu, X. Zhang, L. Wu and P. Dai, Well-designed sunlight-like Bi3+ -activated white-light phosphor for general lighting, *J. Mater. Chem. C*, 2025, **13**, 14856–14863, DOI: 10.1039/D5TC01823D.

47 G. Chen, Y. Qin, Z. Li, X. Wang and Y. Wang, Structure, luminescence properties, and valence-induced spectral behavior of a bismuth-activated garnet phosphor, *J. Mater. Chem. C*, 2024, **12**, 2787–2793, DOI: 10.1039/D3TC04039A.

48 Z. Liao, Q. Zhang, L. Qiu, X. Wei, Y. Chen and M. Yin, CaLuGaO4:Bi3+,Al3+ blue phosphor with excellent thermal stability for multiple LED applications, *J. Mater. Chem. C*, 2025, **13**, 5221–5231, DOI: 10.1039/D4TC05004E.

49 S. Chen, Y. Du, H. Zhao, Y. Yang, Y. Yang, X. Yao, X. Du, J. Wang and R. Yu, Disorder–Order transition and Metal-to-Metal charge transfer induced rare Orangish-Red emission in Bi3 + -Activated double perovskite phosphors, *Chem. Eng. J.*, 2024, **502**, 157928, DOI: 10.1016/j.cej.2024.157928.

50 H. Fei, B. Jing, J. Han, K. Shan, D. Cheng, X. Xu, X. Zhang and J. Wang, Crystal structure, Bi3+ yellow luminescence, and high quantum efficiency of Ba3SbAl3Ge2O14:Bi3+ phosphor for white light-emitting diodes, *Inorg. Chem. Front.*, 2024, **11**, 2616–2625, DOI: 10.1039/D4QI00240G.

51 X. Wu, X. Zhang, Y. Xu, S. Yin, C. Zhong, L. Zhou and H. You, Novel highly efficient Bi3+ -activated phosphors for warm WLEDs, *J. Mater. Chem. C*, 2023, **11**, 8818–8825, DOI: 10.1039/D3TC01396K.

52 X. Zhang, Z. Zhang, Y. Feng, H. Yuan and G. Wang, Luminescence performance of bismuth activated Ba3Lu2B6O15 phosphors, *J. Mol. Struct.*, 2023, **1294**, 136523, DOI: 10.1016/j.molstruc.2023.136523.